RESEARCH ARTICLE

Electromagnetic Analysis and Comparative Study of Surface-Mounted and Consequent Pole Axial Flux Permanent Magnet Machines

RAJESH KUMAR[1], DAE YONG UM[2], (Member, IEEE), LARS SJÖBERG[1], TUSHAR BATRA[1], AND GLYNN ATKINSON[3]

[1]Alvier Mechatronics, 25236 Helsingborg, Sweden
[2]Department of Electrical Engineering, Gyeongsang National University, Jinju-si 52828, Republic of Korea
[3]School of Engineering, Newcastle University, NE1 7RU Newcastle upon Tyne, U.K.

Corresponding author: Glynn Atkinson (glynn.atkinson@newcastle.ac.uk)

ABSTRACT This research presents a comparative analysis of single-sided surface-mounted axial flux permanent magnet (SMAFPM) and consequent-pole axial flux permanent magnet (CPAFPM) machines by evaluating various key electromagnetic parameters. A straightforward replacement of permanent magnets (PMs) with soft magnetic composites (SMCs) is proposed for a conversion of surface-mounted (SM) topology to consequent pole (CP) topology, which maximizes manufacturing ease while sharing the same components. Detailed three-dimensional (3D) finite element analysis (FEA) is performed to assess parameters such as back-EMF, flux-linkage, inductance, torque, and losses. The investigation highlights that despite utilizing 50% less rare-earth permanent magnet (PM) material, the CPAFPM machine produces only 30% less rated torque compared to the SMAFPM machine. However, the CPAFPM machine suffers from reduced magnetic loading and higher armature reaction, leading to 36% lower torque density and reduced efficiency at low speeds and heavy loads. Prototypes of both machines were fabricated, and experimental validation showed a good correlation with the simulation studies. The findings provide insight into the simple conversion to the CPAFPM machine as a viable option for high-speed drives requiring fewer rare-earth PM materials.

INDEX TERMS Axial flux machine, consequent pole, permanent magnet, soft magnetic composites, surface mounted.

I. INTRODUCTION

In the industrial sector, electrical machines contribute 70% of overall energy consumption. This has led to an increased need for highly energy-efficient machines and cost-efficiency achieved in part through miniaturization. The demand is further intensified by regulations mandating minimum energy efficiency levels for new electric motors in major economies, coupled with the ongoing global economic crisis [1], [2]. Permanent magnet machines have emerged as a viable solution to address these challenges; offering extended operational lifespan, enhanced efficiency, superior thermal

The associate editor coordinating the review of this manuscript and approving it for publication was Sinisa Djurovic.

resistance, and reduced size and mass for various industrial applications [3], [4].

PM machines are typically classified into three types based on the direction of the main air-gap flux with respect to the rotational axis: radial flux PM (RFPM) machines, axial flux PM (AFPM) machines, and transverse flux PM (TFPM) machines. The standard off-the-shelf RFPM machine is characterized by bulkier size, lower torque density, and reduced cooling capability, whereas the TFPM machine suffers from a poor power factor, lower efficiency, and manufacturing issues [5], [6], [7]. On the other hand, there has been growing global academic and industrial interest in AFPM machines as an alternative to traditional machines because of their inherent qualities including higher

power density, compactness, direct integration, and thermal stability [8], [9].

The large-scale development of AFPM machines has been hindered primarily by their manufacturing complexities including the necessity for a fully 3-dimensional (3-D) structure – hitherto requiring a complex lamination arrangement for the stator, strong axial magnetic forces [10] all resulting in a high assembly cost. Recent significant advancements in the field of soft magnetic composites (SMC) make high-performance electrical machines with complex 3D geometries feasible for mass production.

SMC is a powder of pure iron particles of diameter 40-400μm (depending on grade) with a nm inorganic coating to provide electrical insulation. Electromagnetic components are formed by pressing the powder with a punch and die, and then subsequently heat treating (below the sintering temperature) to optimize magnetic and mechanical properties. A benefit of this process is electromagnetic 3D net-shape components can be made complete without the need for further machining. The final component exhibits isotropic magnetic, thermal, and mechanical properties. The final components have very good tolerances, high build factor and excellent cost efficiency due to minimal wastage [11], [12]. However, the drawbacks of SMC, such as low permeability, saturation magnetic flux density, mechanical strength, and higher losses at low frequency, can be overcome by selecting proper particle insulation, binder material, pressing direction, and heat treatment processes [13]. The improvement of coating, manufacturing processes, and hysteresis losses for SMC is illustrated in [14]. In [15], the author evaluated the mechanical strength of SMC at 20,000 rpm for an axial flux switched reluctance machine. The impact of temperature on the core losses of SMC is investigated in [16]. The manufacturing methods of single-sided AFPM machines using SMC are discussed in [17].

The majority of axial flux machines (AFMs) employ rare-earth permanent magnets as a source of magnetic potential due to their high energy density. However, there is considerable ongoing debate about reducing reliance on PM materials while retaining the performance advantages over traditional machines, given the cost and volatility of rare-earth PMs. Alternatively, ferrite and Alnico magnets are cost-effective but suffer from poor torque density, while wound-field and induction machines are less efficient and more complex [18], [19]. To decrease the utilization of PM material without sacrificing torque density, the CP topology offers an attractive option, where all the north or south poles of SMAFPM machines are replaced by iron cores. The CPAFPM machines have been widely investigated for various applications [20], [21], [22]. Nevertheless, there are several challenges to overcome in their design to remain competitive in terms of overall machine performance. At the same time, the direct conversion from SM to CP topology should be comprehensively analyzed, benefitting from the pre-compacted SMC parts, which have the potential to

reduce manufacturing efforts and contribute to effective cost reduction.

This paper is devoted to the detailed comparative investigation of the single-sided SMAFPM machine and the CPAFPM machine, focusing on a straightforward replacement of PMs with SMCs. Initially, the key design parameters and machine topologies are presented in Section II. Then, the electromagnetic performance comparison is carried out based on 3-D finite element analysis (FEA) in Section III. Section IV illustrates the fabrication process and experimental validation of two AFPM machine prototypes. Finally, a conclusion is drawn at the end of this paper in Section V.
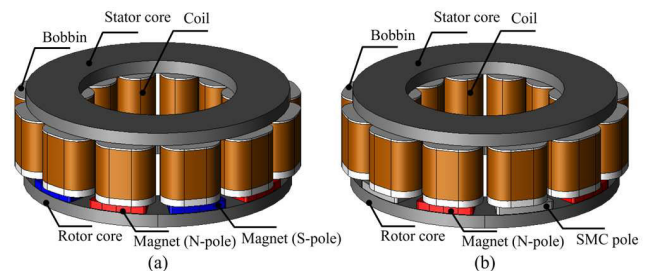

FIGURE 1. The (3D) structure of 12-slot 10-pole. (a) SMAFPM machine. (b) CPAFPM machine.

II. STRUCTURE OF SURFACE MOUNTED AND CONSEQUENT POLE AXIAL FLUX MACHINE

The 12-slot 10-pole single-sided SMAFPM and CPAFPM machines are shown in Fig. 1(a) and (b), respectively. This slot-pole machine with an open slot winding is preferably employed in axial flux topologies due to its superior characteristics in terms of power factor, power density, efficiency, and cogging torque [23], [24]. Both machines use SMC for their stator and rotor cores. The stator is designed with an open-slot configuration to take advantage of net-shape production while using the low-loss Höganäs Somaloy® 700HR-5P with an electrical resistivity of 1250 $\mu\Omega$m and a tensile strength of 20 MPa. Meanwhile, the rotor employs Höganäs Somaloy® 700HR-3P, known for its higher mechanical strength of 65 MPa. Four segmented rare-earth magnets of grade N45SH are glued onto the surface of the rotor. In contrast, the CPAFPM machine topology is created by simply replacing all south poles in the pre-optimized SMAFPM machine with Höganäs Somaloy® Prototyping Material (SPM), using the same assembly process as gluing PMs for manufacturing ease [25]. The key design parameters of both topologies are shown in Table 1.

The 12-slot configurations have an ortho-cyclic double-layer concentrated winding with 4 coils/phase in a three-phase arrangement, where the number of turns in each coil is 62. The fractional slot concentrated winding, as depicted in Fig. 2(a), offers advantages of shorter end winding length, improved fault tolerance, and efficient space utilization compared to distributed winding [26]. Moreover, the coils can be pre-wound in bobbins, enhancing both manufacturing

TABLE 1. Design results of the optimized SMAFPM machine.

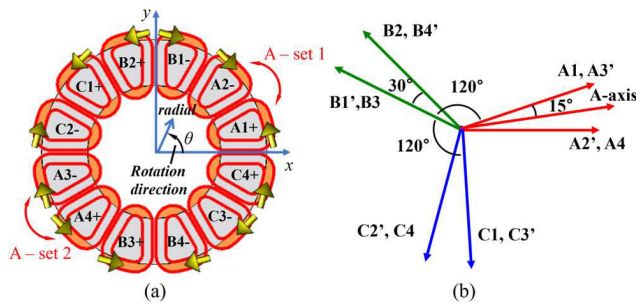| Parameter	Value
Stator outer diameter (mm)	109.7
Stator inner diameter (mm)	50.3
Axial length (mm)	37.3
Air gap length (mm)	1
Slot/pole	12/10
PM thickness (mm)	3.1
PM span - electrical angle (°)	130
Number of turns per slot	62
Rated speed (r/min)	6,000
Rated line current – Amplitude (A)	12.07
Rated current density – RMS (A/mm²)	5

FIGURE 2. The winding layout of 12-slot and 10-pole machines. (a) The coil arrangement. (b) Phase vector diagram.

FIGURE 3. The cross-sectional view, MMF from PMs, and permeance waveforms. (a) SMAFPM machine (b) CPAFPM machine.

ease and the filling factor. Two adjacent coils are wound anti-periodically and arranged into a coil set (A-set 1: A1+ & A2− / A-set 2: A3− & A4+). The phase vector diagram shown in Fig. 2(b) defines the d-axis as the N-pole aligned with the A-axis in the rotor reference frame.

The cylindrically sliced cross-sectional view at the mean radius of the SMAFPM and CPAFPM machine is presented in Fig.3 (a) and (b). From this view, the inherent characteristics of each topology can be qualitatively derived by distribution of magneto-motive force (MMF) from PMs $F_{PM}(\theta_s)$, permeance of stator $\Lambda_s(\theta_s)$ and rotor $\Lambda_r(\theta_s)$.

Note that θ_s is stator position referring to the center of a stator teeth, θ_r is rotor position referring to the center of N-pole, and θ_m is the rotation angle of the rotor. The distribution of MMF from PMs can be written in the form of Fourier series as follows:

$$F_{PM}(\theta_s) = F_0 + \sum_{n=1}^{\infty} F_n \cos(np(\theta_s - \theta_m)) \quad (1)$$

where F_0 is the offset component and F_n is n-th harmonic component F_{PM}, which are determined by the material of PMs and SMCs, pole arc ratio of the magnet α and SMC pole β. The air-gap permeances due to the stator and rotor structure can be expressed as

$$\Lambda_s(\theta_s) = \Lambda_{s0} + \sum_{k=1}^{\infty} \Lambda_{sk} \cos(kN_s\theta_s) \quad (2)$$

$$\Lambda_r(\theta_s) = \Lambda_{r0} + \sum_{k=1}^{\infty} \Lambda_{sk} \cos(np(\theta_s - \theta_m)), \quad (3)$$
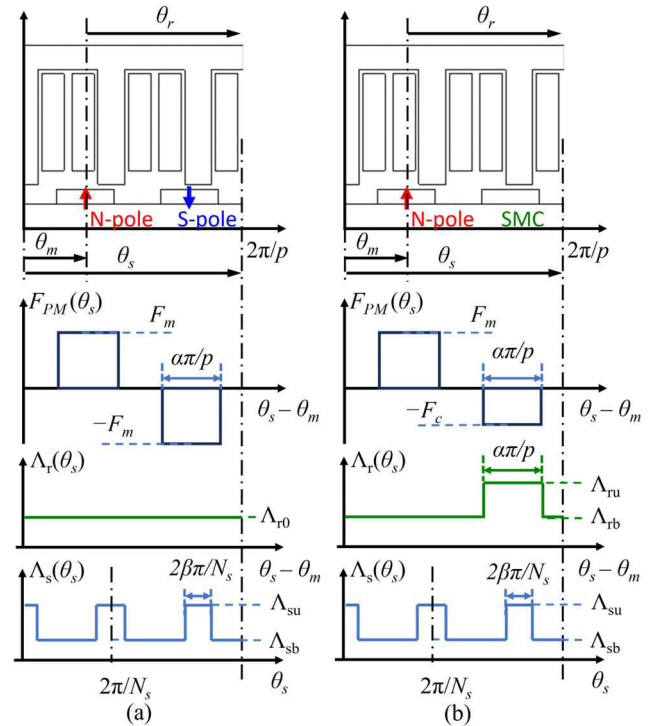
respectively, where Λ_{s0} and Λ_{r0} are average components, the k-th harmonic components of stator and rotor permeance are $\Lambda_{sk} = \frac{2}{\pi k}(\Lambda_{su} - \Lambda_{sb})\sin(k\pi\beta)$ and $\Lambda_{rk} = \frac{2}{\pi k}(\Lambda_{ru} - \Lambda_{rb})\sin(\frac{k\pi\alpha}{2})$ where α is pole arc ratio and $(1-\beta)$ is slot opening ratio.

Multiplying (1), (2) and (3), limitedly considering the offset and fundamental components of F_{PM}, Λ_s, and Λ_r, can derive the magnetic field due to PMs, written by

$$\begin{aligned} B_{PM}(\theta_s) &= F_{PM}(\theta_s)\Lambda_s(\theta_s)\Lambda_r(\theta_s) \\ &= F_1\Lambda_{s0}\Lambda_{r0}\cos(p(\theta_s - \theta_m)) \\ &\quad + \frac{F_1\Lambda_{s1}\Lambda_{r0}}{2}\cos(p(\theta_s - \theta_m) \pm N_s\theta_s) \\ &\quad + \frac{F_1\Lambda_{s0}\Lambda_{r1}}{2}\cos(2p(\theta_s - \theta_m)) \\ &\quad + \frac{F_1\Lambda_{s1}\Lambda_{r1}}{4}\{\cos(2p(\theta_s - \theta_m) \pm N_s\theta_s) \\ &\quad + 2\cos(2N_s\theta_s)\}. \end{aligned} \quad (4)$$

For the SMAFPM topology, Λ_{r1} can be set as zero so this machine exhibits p and $(p \pm N_s)$-th harmonic components in the air-gap flux density. In contrast, for the CPAFPM topology, SMC poles generate Λ_{r1}, resulting in additional $2p$, $2p \pm N_s$, and $2N_s$-th harmonic components. These double harmonics of pole-pairs are the origin of back-electromotive force (EMF), torque, iron losses, and magnet eddy current losses, exhibiting distinct characteristics compared to SMAFPM machine.

III. ELECTROMAGNETIC PERFORMANCE

The 3D FEA analysis of the aforementioned machine models is conducted in JMAG software for detailed performance evaluation at various operating points mentioned in Table 2. The magnet flux-linkage, cogging torque, and back-EMF are studied at room temperature and compared between the SMAFPM and CPAFPM topologies. Additionally, load-dependent inductance, torque, and losses are computed at the temperatures defined in Table 2 to assess the overload and high-speed performance capabilities of both machines. Furthermore, the efficiency diagram is generated under different working conditions, accounting for all power losses while omitting mechanical and switching losses.

TABLE 2. Four operating conditions of for load analysis.

Parameter	OP1	OP2	OP3	OP4
Output power (W)	140	1,700	1,650	1,790
Torque (Nm)	1.37	2.71	5.25	1.90
Rotating speed (r/min)	1,000	6,000	3,000	9,000
Coil temperature (°C)		120		
Magnet temperature (°C)		80		

A. AIR-GAP FLUX DENSITY AND FIELD DISTRIBUTION

The open-circuit magnet flux density distribution of the stator and rotor cores at 1,000 rpm is displayed in Fig. 4(a) and (b). To represent the open-circuit condition where machines are normally tested, the PM temperature and remanence are set at 20°C and 1.35 T, respectively. The SMAFPM machine, shown in Fig. 4(a), exhibits a symmetric distribution of the flux density below 1.4 T, which is well-designed with the typical magnetic loading of AFPM machines using SMC cores. In contrast, the CPAFPM machine shows a notably asymmetric distribution in the stator tooth (left: 1.04 T/right: 0.84 T) due to the larger leakage flux of the magnet and lower flux density compared to the SMAFPM machine. This results in higher electrical loadings due to the lower magnetic loading for the same rating.

The axial (z) component of air-gap flux density along the circumferential direction at the mean radius for the mechanical cycle is presented in Fig. 5 (a) and (b), which show agreement with the theoretical spectra predicted in (4). The harmonic components due to the contribution of slot-pole combination are obtained by Fast Fourier Transform (FFT). Both topologies contain the 5th harmonic component of pole-pair, 7th & 17th harmonics due to the stator slotting effect, and the 15th harmonic component (3×pole-pair) relying on the magnet shape and its magnetization distribution. Unlike the SMAFPM topology, the CPAFPM machine exhibits a 34% lower 5th harmonic component of 0.54 T due to the 50% lower magnet mass. Notably, the 10th harmonic component (2×pole-pair) can be seen in Fig. 5(b) and be reflected in the flux-linkage and back-EMF.
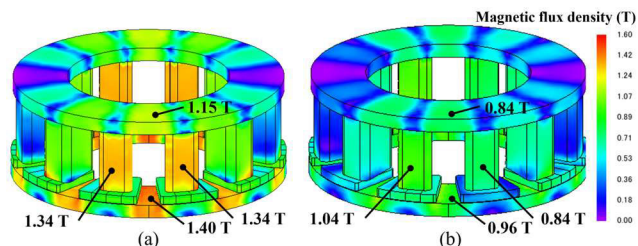

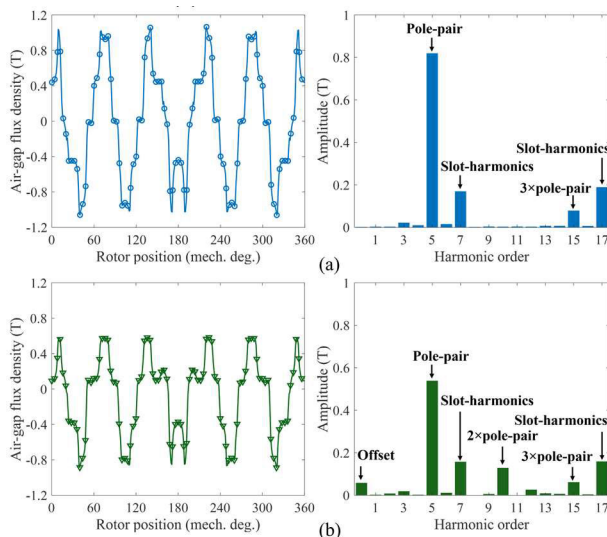**FIGURE 4.** Flux density at 1,000 rpm under open-circuit condition. (a) SMAFPM machine. (b) CPAFPM machine.

FIGURE 5. Open-circuit air gap flux density in axial (z) direction. (a) SMAFPM machine. (b) CPAFPM machine.

B. MAGNET FLUX-LINKAGE AND BACK-EMF

For one electrical cycle, the PM flux linkage and back-EMF of A-phase coil is shown in Fig. 6 (a) and (b). The CPAFPM machine has a lower peak of the flux-linkage waveform with a 30% lower fundamental component compared to the SMAFPM machine. The waveforms of each coil set do not overlap in the CPAFPM topology, indicating that out-of-the phase 2nd harmonic components lead to the voltage difference between coil sets. Consequently, the back-EMF across each coil set in the CPAFPM machine has a 30% lower fundamental component than that of SMAFPM machine, the 2nd and 3rd harmonics of 7% and 6.5%, compared to the fundamental component, respectively.

The inclusion of harmonics should be carefully considered in the design stage to mitigate the torque ripple and additional losses. Fig. 7(a) and (b) show circulating currents flowing in A-phase winding where coils are connected in series and parallel, respectively. The delta connection is employed to analyze the impact of the circulating current from both 2nd and 3rd harmonics. The only 3rd harmonic currents can be seen in series coils while the additional 2nd harmonic currents flow in parallel coils of the CPAFPM machine.

For the phase coil connection of 12-slot 10-pole CPAFPM machines, two sets of phase coils (A-set 1 and A-set 2) should be connected in series to eliminate the 2nd and
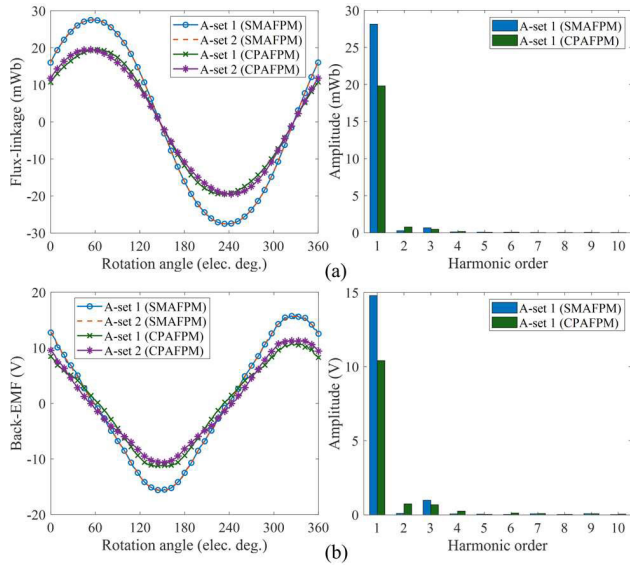
FIGURE 6. Comparison of SMAFPM and CPAFPM machines. (a) Magnet flux-linkage. (b) Back-EMF across A-phase coil sets.
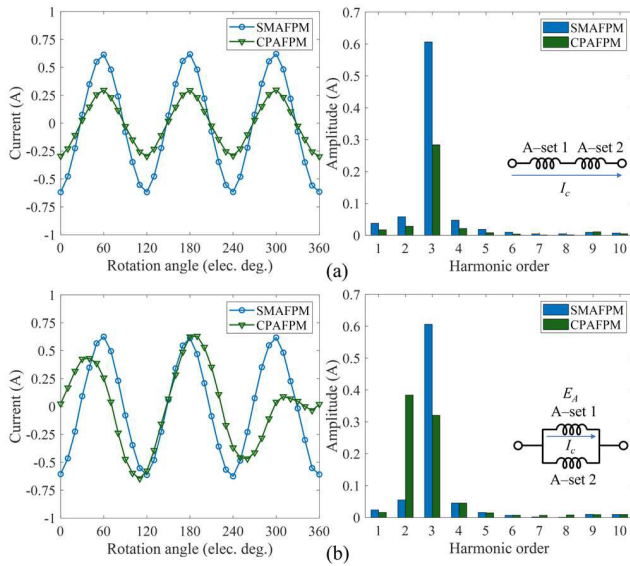

FIGURE 7. Circulating currents in the delta connection at 1,000 rpm. (a) In series. (b) In parallel.
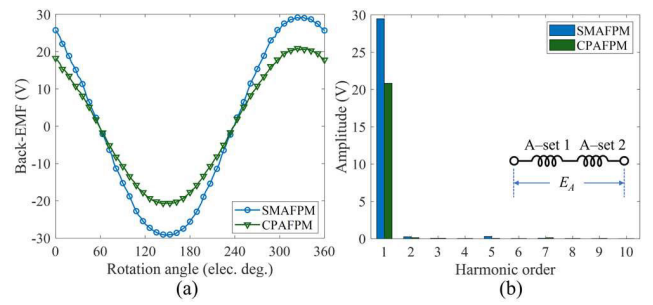

FIGURE 8. Back-EMF waveforms and their harmonic components with series connected delta winding at 1,000 rpm. (a) SMAFPM machine. (b) CPAFPM machine.
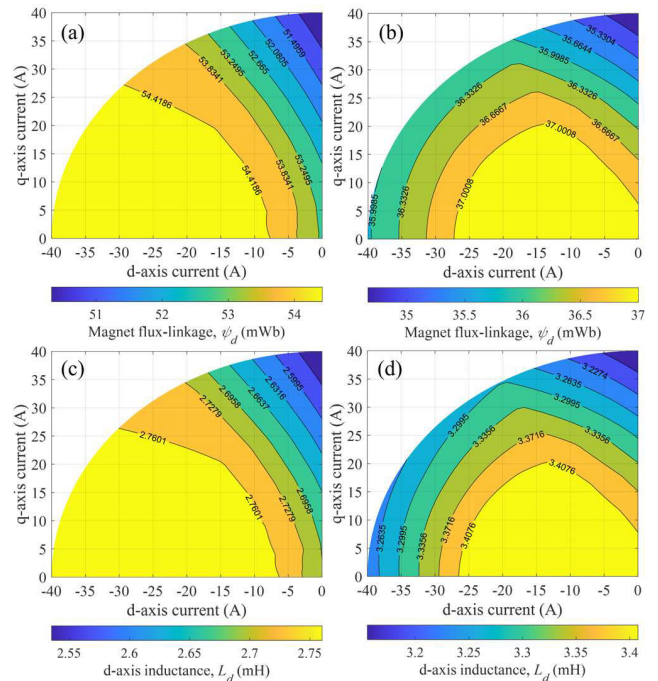

FIGURE 9. Load-dependent maps. (a-b) Magnet flux-linkage of SMAFPM CPAFPM machines, respectively. (c-d) D-axis inductance map of SMAFPM and CPAFPM machines, respectively.

higher even-harmonics, as presented in Fig. 8. Based on the analysis, the delta connection with each phase coil in series is selected as a winding configuration for the detailed comparative investigation between SMAFPM and CPAFPM machine topologies.

C. LOAD-DEPENDENT FLUX-LINKAGE & INDUCTANCE

The effective length of the airgap, g_e, for single sided AFPM machines is represented as

$$g_e = g + k_m \frac{L_m}{\mu_{mr}} \qquad (5)$$

where g is the mechanical air-gap, L_m is the magnet thickness, μ_{mr} is the relative permeability of the PM, and k_m is a factor that is 1 for SMAFPM machines and 0.5 for CPAFPM machines [27]. This is mainly due to a decreased air-gap in the CPAFPM topology compared to the SMAFPM machine, leading to variations in armature inductance and subsequent load-dependent properties.

The magnet flux-linkage and inductance maps on the d-axis and q-axis line currents presented in Fig. 9 (a-d) are obtained using frozen permeability methods, considering cross-saturation due to q-axis currents [28]. The current density for 40 A is 16.6 A/mm^2, which is sufficient to demonstrate the overload capability of the two topologies. The CPAFPM machine has lower magnet flux-linkage across all current combinations, indicating that higher q-axis current is required to achieve the same average torque. In contrast, the

inductances of the CPAFPM machine are 1.26 times higher than those of the SMAFPM machine, increasing the effects of armature reaction on magnetic saturation and line-voltage increment.
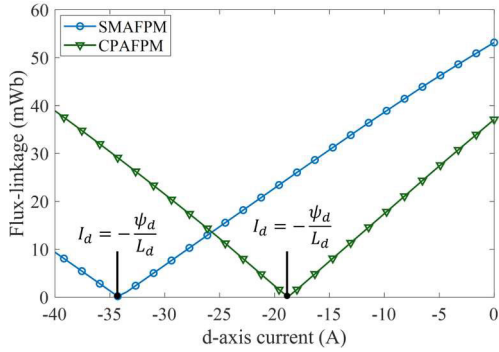

FIGURE 10. Net flux-linkage at different d-axis currents ($I_q = 0$).
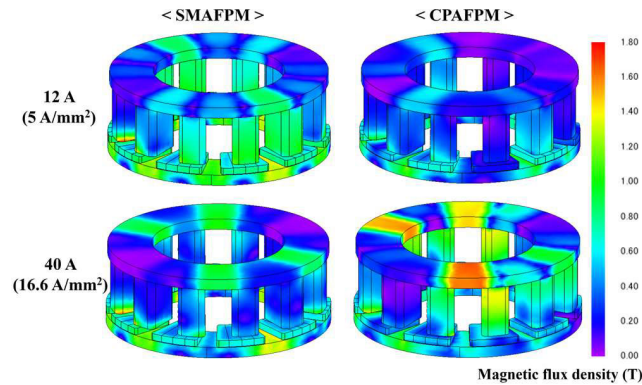

FIGURE 11. Flux density distribution on stator and rotor cores at two different d-axis currents ($I_d = 12$ A and $I_d = 40$ A) with $I_q = 0$.

The difference in contours between the two machine geometries is visible at higher negative d-axis currents, where the net flux-linkage is fully compensated (referred to as the characteristic current). Conversely, the net flux-linkage increases in the reverse direction when the demagnetizing flux exceeds the magnet flux, as shown in Fig. 10. The magnet flux-linkage and characteristic current of the CPAFPM machine are 30% and 45% lower than those of the SMAFPM machine, respectively. Thus, the CPAFPM machine is more advantageous for higher speeds and light loads in terms of constant power operation through flux-weakening control compared to the SMAFPM machine. Furthermore, the effect of d-axis currents on the flux density distribution of the two machines can be seen in Fig. 11. The d-axis current below the characteristic current prevents the cores from reaching saturation. However, when the demagnetizing flux exceeds the magnet flux-linkage, the stator core becomes susceptible to saturation due to leakage flux. This is the main indication of the decreasing trends in Fig. 9(d), which cannot be seen in Fig. 9(c).

The overload capability of PM machines depends on how sharply the magnet flux-linkage decreases with increasing electric loadings (current density), leading to a lower torque constant. In Fig. 12(a), the magnet flux-linkage is not highly sensitive to the q-axis currents up to the current density of 15 A/mm^2, demonstrating high overload capability. This is due to thick magnets and a wide air-gap, reducing the total magnetic reluctance of the machine's magnetic circuit and making it less sensitive to the permeability of stator and rotor cores. Additionally, the SMAFPM machine has a wider effective air-gap of 3.9 mm compared to 2.4 mm for the CPAFPM machine, as observed in Fig. 12(b). This difference is 5.5% for SMAFPM and 6.5% for CPAFPM machines, respectively. Fig. 13 illustrates the impact of armature reaction on magnetic saturation, resulting in a steeper decline of the magnet flux-linkage in the CPAFPM machine. Despite the lower magnet flux of the CPAFPM machine, the flux density is susceptible to increase due to armature currents. This characteristic makes the CPAFPM topology less favorable for overload operations.
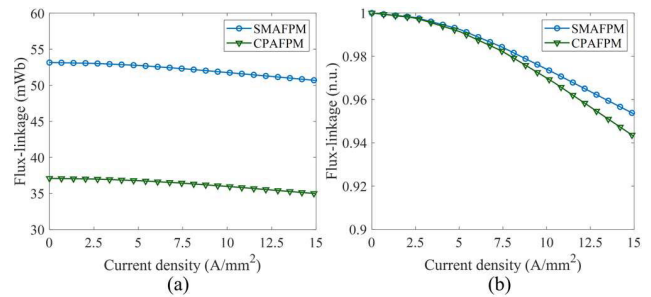

FIGURE 12. Flux linkage comparison. (a) Magnet flux-linkage. (b) Normalized magnet flux-linkage against the current density at different currents ($I_d = 0$).
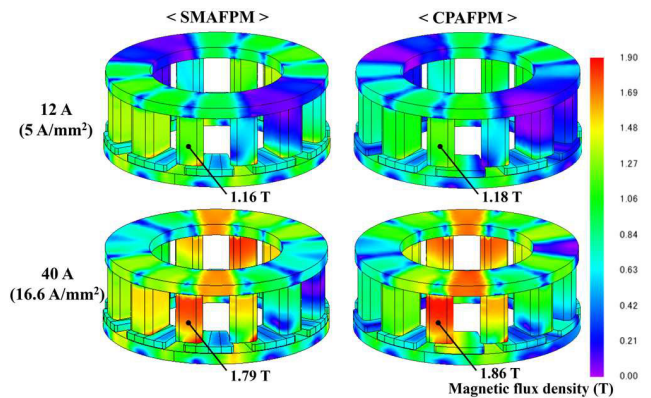

FIGURE 13. Flux density distribution on stator and rotor cores at two different q-axis currents ($I_q = 12$ A and $I_q = 40$ A) with $I_d = 0$.

The dependence of electric loadings on d-axis and q-axis inductance can be seen in Fig. 14. The SMAFPM machine has almost no saliency characteristic of surface mounted (SM) machines. Similarly, the CPAFPM, which employs SMC poles and half magnets, lacks significant saliency. However,
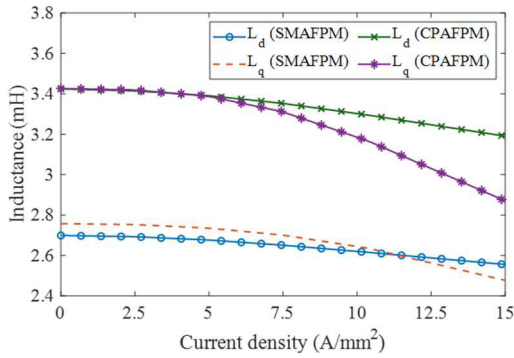
FIGURE 14. D-axis and q-axis inductances against the current density at different currents ($I_d = 0$).

the armature field generated from q-axis current lowers q-axis inductance and increases the saliency. Therefore, unlike SMAFPMM machines, the existence of SMC poles can make the saliency. This result gives an opportunity for CPAFPM machines to facilitate the reluctance torque.

D. TORQUE CHARACTERISTICS

The cogging torque of the two machines under open-circuit operation, presented in Fig. 15 (a) and (b), exhibits a 12th harmonic waveform within one electrical period. The number of cogging torque cycles in one mechanical rotation is 60 (12 cycles in one electrical period), attributed to the least common multiple of the pole-pair of 5 and the number of slots of 12. The amplitude of cogging torque is 0.06 Nm and 0.027 Nm for the SMAFPM and CPAFPM machines, respectively.
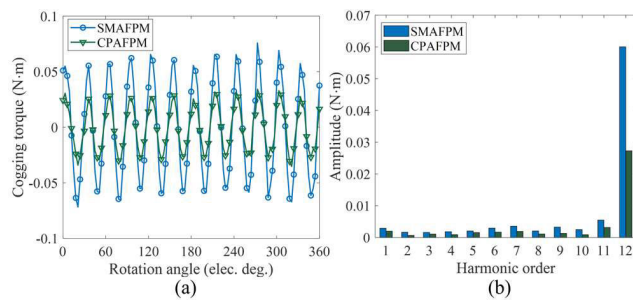

FIGURE 15. Cogging torque of SMAFPM and CPAFPM machines. (a) Waveforms. (b) Harmonic components.

The electromagnetic torque is studied and compared at a speed of 1,000 rpm with a line current of 6A. In Fig. 16 (a) and (b), the CPAFPM machine exhibits 70% of the average torque of the SMAFPM machine. This corresponds with the difference in back-EMF between the two topologies, as introduced in Section III-B. The torque waveform includes 12th harmonics, and the torque ripples of the SMAFPM and CPAFPM machines are 0.14 Nm and 0.08 Nm, respectively. This indicates that the main contribution of torque ripple is from cogging torque, where peak-to-peak values are 0.12 Nm and 0.054 Nm, respectively. Additionally, the average torque
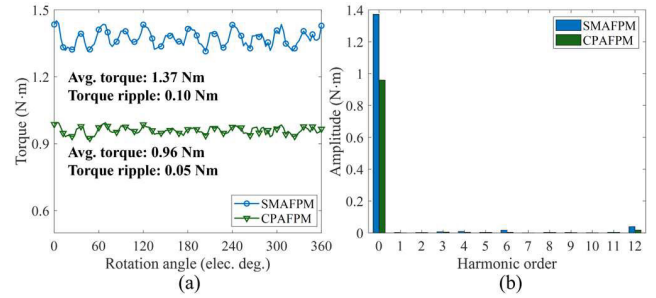

FIGURE 16. Torque comparison of SMAFPM and CPAFPM machines at 1,000 rpm and 6 A line current. (a) Waveforms. (b) Harmonic components.
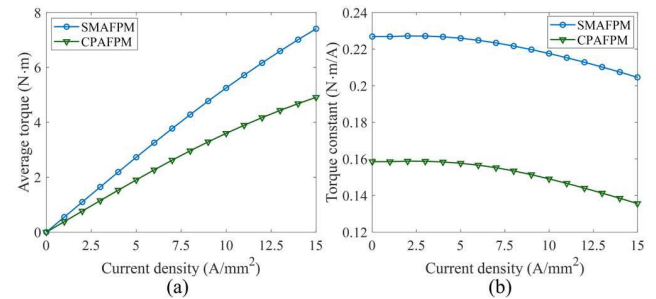

FIGURE 17. Average torque vs current density. (b) Torque constant against the current density at different currents (Id = 0).

of the SMAFPM and CPAFPM machines is calculated at different q-axis currents and plotted in Fig. 17 (a) and (b). The CPAFPM machine shows a 30% lower torque constant at a current density of 2.5 A/mm^2, and a 34% lower torque constant at 10 A/mm^2, attributed to magnetic saturation. To achieve the same torque production as the SMAFPM machine at 2.5 A/mm^2, the CPAFPM machine would require a 44% higher current. However, to achieve the torque of the SMAFPM machine at 10 A/mm^2, the CPAFPM machine would require a 66% higher current. The higher armature reaction of the CPAFPM topology, discussed in Section III-C, can make the machine susceptible to deep saturation due to higher armature inductance, leading to poorer overload capability compared to the SM topology.

E. POWER FACTOR

The dependence of the power factor on electric loadings can be seen in Fig. 18(a). The CPAFPM machine has an inherent weakness of a low power factor due to lower magnetic loading and higher armature inductance. The power factor degrades from 0.97 to 0.74 for the CPAFPM machine, but only from 0.99 to 0.89 for the SMAFPM machine, as the current density increases from 2.5 to 10 A/mm^2. Moreover, for the same torque production of 1.5 Nm and 4.5 Nm, the CPAFPM machine exhibits power factors of 0.93 and 0.67, respectively, while the SMAFPM machine shows power factors of 0.99 and 0.91, respectively. Consequently, a higher inverter rating is needed to employ the CPAFPM topology.
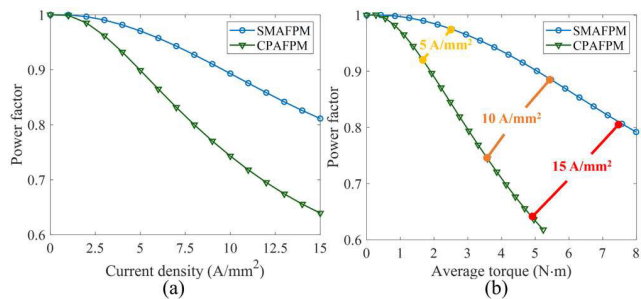
FIGURE 18. Power factor comparison for two machines. (a) Power factor against current density ($I_d = 0$). (b) Power factor against average torque ($I_d = 0$).

FIGURE 19. Torque-winding loss curves ($i_d = 0$).

F. POWER LOSSES AND EFFICIENCY

The winding loss and associated torque level are displayed in Fig. 19. For the same torque production of 1.5 Nm and 4.5 Nm, the winding losses of the CPAFPM machine are 19.06 W and 220.75 W, which are 2 and 2.47 times higher than the 9.45 W and 89.39 W of the SMAFPM machine, respectively. The higher current density negatively impacts the CPAFPM machine, making it unsuitable for high-torque and low-speed applications where winding losses dominate over iron losses.

The speed dependent iron and magnet eddy current losses are compared at different current densities of 2.5 and 10 A/mm^2. The iron loss of SMC cores was calculated by employing the Steinmetz equation [26]:

$$p_{iron} = p_{bulk} + K_h\,(f_n, B_n)\,f_n + K_e\,(f_n, B_n)\,f_n^2 \qquad (6)$$

where p_{iron} is the iron loss density (W/kg), p_{bulk} is the inter-particle joule loss density in SMC cores, f_n is the frequency of n-th harmonic component, B_n is the nth harmonic amplitude of flux density, $K_h\,(f_n, B_n)$ is the hysteresis loss coefficient, and $K_e\,(f_n, B_n)$ is the intra-particle eddy current loss coefficient.

At a current density of 2.5 A/mm^2, the CPAFPM machine demonstrates lower iron loss, as shown in Fig. 20(a). However, at a higher current density of 10 A/mm^2, the iron losses increase significantly more than in the SMAFPM machine, attributed to the stronger armature field in the CPAFPM machine. Furthermore, the 50% lower magnet mass in the CPAFPM machine reduces magnet eddy current losses even under high loading conditions of 10 A/mm^2, as illustrated in Fig. 20(b). This reduction is due to the substantial leakage of armature fields through the rotor, diminishing their effect on the magnets. Additionally, machine models with four segmented magnets further decrease the impact of magnet eddy current loss on the total loss. Nonetheless, the CPAFPM machine is expected to excel in high-speed operations, offering reduced thermal risks to the magnets across a broad range of operating conditions.

For the comparison of losses under identical torque and speed conditions, speed-torque-loss maps were calculated within a torque range of 0 to 5.4 Nm and a speed range of 0 to 10,000 rpm. The q-axis and d-axis currents were adjusted to
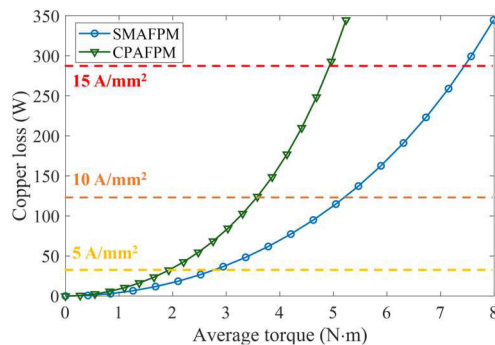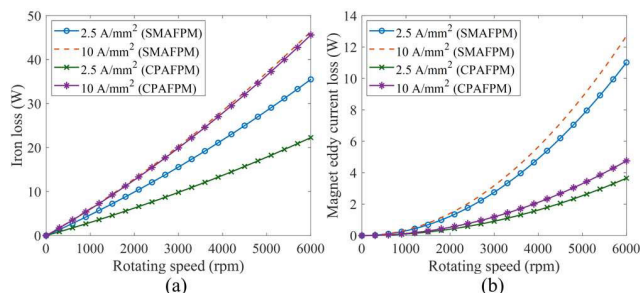

FIGURE 20. Speed-dependent losses at 2.5 A/mm^2 and 10 A/mm^2 ($I_d = 0$). (a) Iron loss. (b) Magnet eddy current loss.

identify the operating point with the highest efficiency. The winding loss maps include AC winding losses, which result in higher losses at higher speeds for the same torque due to the rotating magnets. This effect is evident at high-speed, low-torque operating points in Fig. 21(a), indicating that the impact of AC loss is greater for the SMAFPM machine because of its higher magnet flux. Consequently, the winding loss of the CPAFPM machine in Fig. 21(b) is comparable to that of the SMAFPM machine during high-speed operation with low loads, despite its higher current excitation.

Moreover, the sum of the iron loss and magnet eddy current loss is strongly dependent on the rotating speed, as represented by the vertical contour lines in the speed-torque maps in Fig. 21(c) and (d). The CPAFPM machine exhibits lower losses in the low-torque region due to its lower magnetic loading. However, higher losses are observed at high torque production, even in the high-speed region, due to the high armature fields. To summarize the loss maps, the higher efficiency of the CPAFPM machine is expected primarily during high-speed operation with low loadings, where the iron loss is not substantially affected by the armature reaction, and the winding loss is comparable to the iron loss and magnet eddy current loss.

The efficiency maps in Fig. 22 are obtained from the data in loss maps by neglecting current and voltage constraints for investigating the performance across a wide range of ratings.

The white dotted lines, connecting the same current density of 5, 10, and 15 A/mm^2, overlap in the map to represent the trajectory of the electric loadings in terms of maximizing efficiency at each rotating speed. The line for 5 A/mm^2

TABLE 3. Performance of The SMAFPM and CPAFPM Topologies at Four Operating Points.

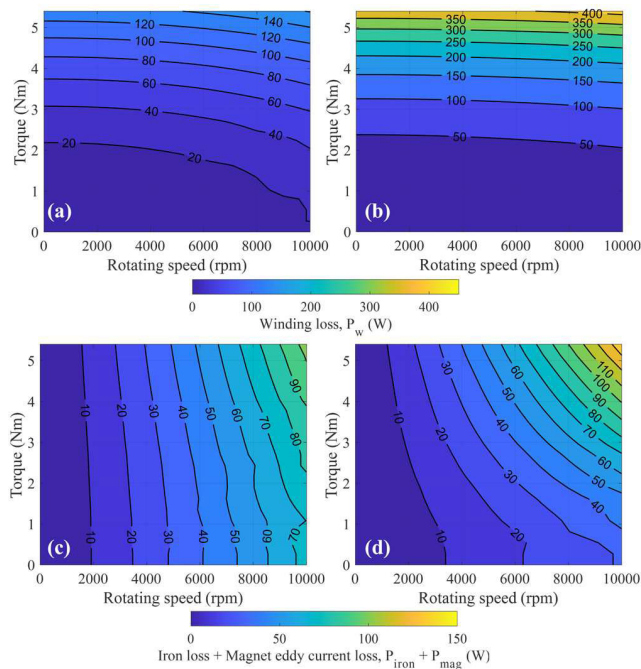| Parameter	SMAFPM machine				CPAFPM machine			
	OP1	OP2	OP3	OP4	OP1	OP2	OP3	OP4
Line current - Amplitude (A)	6.11	12.74	24.28	10.44	8.72	17.97	41.35	12.89
Current density - RMS (A/mm^2)	2.53	5.28	10.06	4.32	3.61	7.44	17.13	5.34
Current angle (º)	9.2	18.7	6.4	36.9	4.4	14.7	14.3	20.6
Line voltage – Amplitude (V)	28.90	161.58	97.65	218.69	22.67	139.13	107.91	175.19
Torque ripple (%)	9.08	4.34	2.32	7.01	5.11	2.88	3.05	4.49
Power factor	0.999	0.999	0.917	0.904	0.965	0.869	0.603	0.969
Stator iron loss (W)	4.39	31.53	18.15	44.98	2.82	26.44	23.53	33.33
Rotor iron loss (W)	0.15	1.40	1.07	1.83	0.40	5.18	4.34	6.35
Magnet eddy current loss (W)	0.30	10.04	2.99	20.22	0.10	4.40	1.31	6.99
Winding loss (W)	8.30	39.27	129.32	33.62	16.64	72.93	378.89	42.47
Total loss (W)	13.13	52.24	151.53	100.65	19.96	108.96	408.06	89.14
Efficiency (%)	91.67	95.48	91.69	94.73	87.88	94.00	80.46	95.28

FIGURE 21. Speed-torque-loss maps: (a-b) The winding loss for SMAFPM & CPAFPM machines, respectively. (c-d) The sum of iron loss and eddy current loss for SMAFPM & CPAFPM machines, respectively.

shifts toward the lower torque region as the rotating speed increases due to the additional d-axis current needed to attain the highest efficiency by balancing winding loss and iron loss. The higher efficiency over 95% is found in the higher torque region between 5 and 10 A/mm^2 for the SMAFPM machine, while the CPAFPM machine offers an efficiency of over 95% at high speeds (>6,000 rpm) and in the low torque region of around 5 A/mm^2.

The detailed power loss and efficiency comparison of four operating points (OP1, OP2, OP3, and OP4), introduced previously, is presented in Table 3. At the low torque of

1.37 Nm and low-speed point of 1,000 rpm (OP1), 44% more current is required to achieve the same torque for the CPAFPM machine, resulting in double the winding loss. Consequently, the winding loss dominates at this operating point, leading to the efficiency of the CPAFPM machine being 3.75% lower than that of the SMAFPM machine. At a higher speed of 6,000 rpm and a rated torque of 2.71 Nm (OP2), the iron loss and magnet eddy current loss account for a similar portion of the winding loss, narrowing the efficiency difference between the two topologies. Additionally, a larger efficiency difference of over 11% is found around the overload torque of 5.25 Nm and a speed of 3,000 rpm (OP3). The high armature reaction of the CPAFPM machine negates the benefit of low iron loss, and its low power factor, along with substantial winding loss, demonstrates its poor overload capability.

In contrast, the CPAFPM machine achieves the highest efficiency at a speed of 9,000 rpm and around a rated torque of 1.9 Nm. The lower magnetic loading with reduced magnet usage is advantageous at higher speeds for the same output power, benefiting from lower iron loss and magnet eddy current loss. The results at operating points OP2 and OP4 demonstrate that the SMAFPM and CPAFPM machines exhibit similar performance at a current density of around 5 A/mm^2, with a similar output power of 1,700 W and 1,790 W, respectively. Therefore, for AFPM machines designed for a given output power, where an additional gearbox is included in the system, the CPAFPM topology can be flexibly targeted toward higher speeds and lower torque. This is due to its low iron loss, reduced magnet eddy current loss, and reduced use of magnets.

IV. PROTOTYPING AND EXPERIMENTAL VALIDATION

This section offers a concise overview of SMAFPM and CPAFPM machines prototyping, manufacturing challenges, and the correlation between simulated and measured results.
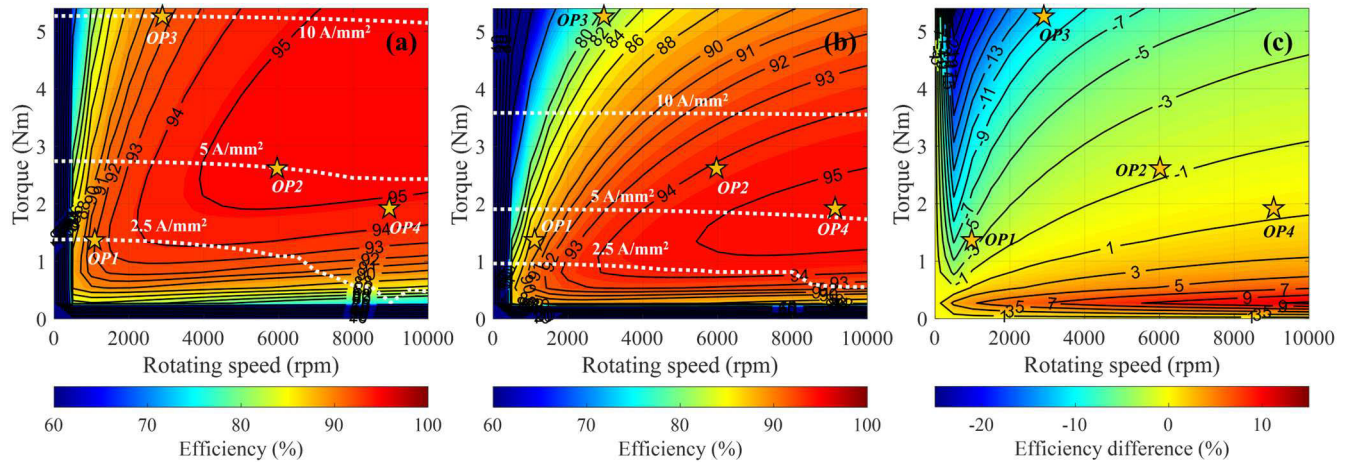
FIGURE 22. Efficiency maps for (a) SMAFPM and (b) CPAFPM machines, and the difference of efficiency between two topologies.

The 3D FEA analysis of the aforementioned machine models is conducted in JMAG software for detailed performance evaluation at various operating points mentioned in Table 2. The magnet flux-linkage, cogging torque, and back-EMF are studied at room temperature and compared between

A. PROTOTYPE DEVELOPMENT

The SMC based prototypes utilize the size-dependent single stator component concept, considering an 800-ton press, where the stator is pressed in a single operation, saving manufacturing and assembly costs with zero wastage. The stator made from the Höganäs Somaloy® 700HR 5P-40 mesh material features 12 open teeth, facilitating ease in winding directly on the bobbins and slotting them onto the teeth with a better fill factor. There are 62 copper wire turns wound on each coil bobbin made of 3D-printed plastic PA 3200 GF material. The copper wire, classified as temperature class H and enamel grade 2, has an outer diameter of 1.2 mm. The series connected four coils/phase are arranged in delta winding scheme. Furthermore, the whole stator assembly is supported by aluminium 6082 housing. The complete stator assembly is shown in Fig. 23.
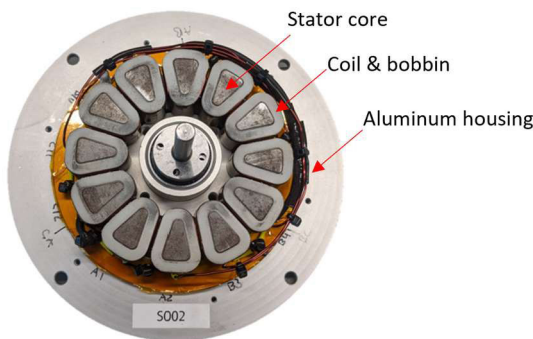

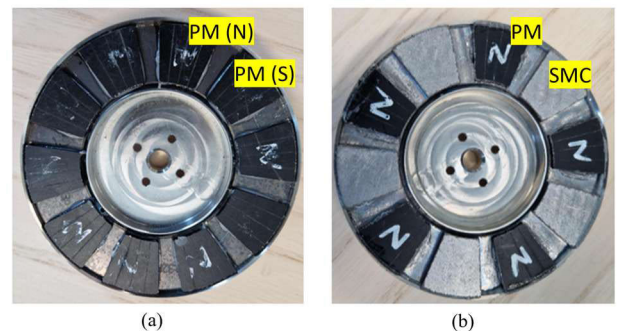**FIGURE 23.** Complete stator assembly of SMAFPM and CPAFPM machines.

FIGURE 24. Rotor assembly. (a) SMAFPM machine. (b) CPAFPM machine.

The rotor core is constructed from high-strength Höganäs Somaloy® 700HR 3P-40 mesh material. PERMABOND® ET5401 epoxy serves as the adhesive for affixing 10 magnets onto the rotor surface. The neodymium magnets of grade N45SH are segmented into four parts to reduce losses, especially eddy current losses. Similarly, the rotor assembly is also supported by aluminium holding as depicted in Fig. 24. In addition, the south poles of the SMAFPM motor are replaced by SPM material for manufacturing simplicity in prototyping.

B. MEASUREMENT vs 3-D FEA SIMULATIONS

The prototyped machines are validated using the test setup depicted in Fig. 25. The test motor is connected to the torque transducer, which is shared with the servo drive. Initially, the measurement of back-EMF and static torque are performed to ensure the fidelity of the 3-D FEA model under study. Then, on-load performances are measured to compare torque, losses, and efficiency. These dynamic tests are carried out at different loads and speeds of 1,000 rpm and 2,000 rpm. However, validation at higher speeds is not included due to the limitations of the testing environment.
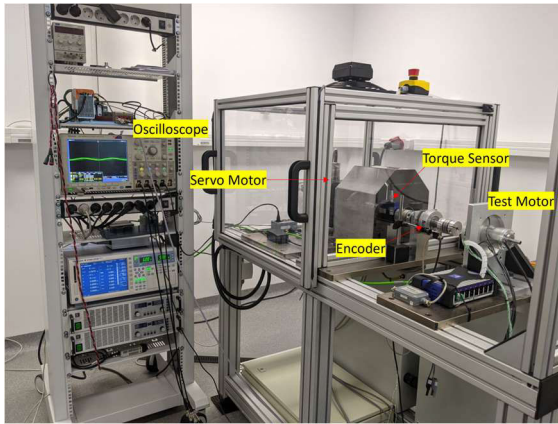
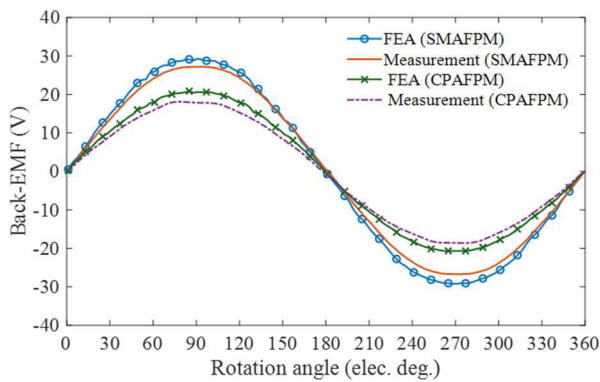**FIGURE 25.** Test setup of the SMAFPM and CPAFPM machines under study.

FIGURE 26. Comparison of back-EMF obtained from FEA and measurement at the speed of 1,000 rpm.

1) BACK-EMF AND STATIC TORQUE MEASUREMENT

Fig. 26 presents back-EMF waveforms obtained at the speed of 1,000 rpm. The fundamental harmonic amplitudes from 3-D FEA are 29.49 for the SMAFPM machine and 20.84 V for the CPAFPM machine, representing a 29.3% difference. The measured back-EMF is 27.34 V and 18.39 V for SMAFPM and CPAFPM machines, respectively.

The static torque waveforms are evaluated and compared in Fig. 27. For static torque testing, two terminals of the delta-connected winding are fed by a DC power supply to obtain line-current of 10 Adc. As a result, the currents injected into each phase winding are 6.67 Adc for one phase winding and −3.33 Adc for other phase windings. The torque waveforms between 3-D FEA and measurement are aligned by 2.78 Nm and 2.61 Nm at the rotor angle of 90° (q-axis) for the SMAFPM machine. The CPAFPM machine show lower torque that can be seen in both FEA and measured waveforms.

In Table 4, the difference between measurements and simulations results from the deviation between the B-H curves of the manufactured SMC core and the datasheet. Additionally, the CPAFPM prototype shows a higher difference due to some defects, such as irregular surfaces and cracks on
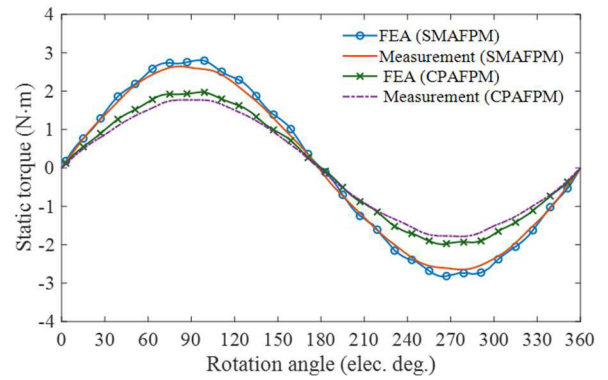

FIGURE 27. Comparison of the static torque obtained from FEA and measurement.

TABLE 4. Comparison of Back-EMF and static torque.

Parameter	Back-EMF (Fundamental)		Static torque (At 90 elec. deg.)	
	SMAFPM	CPAFPM	SMAFPM	CPAFPM
Measurement	27.34 V	18.39 V	2.78 Nm	1.95 Nm
3-D FEA	29.49 V	20.84 V	2.61 Nm	1.78 Nm
Difference	7.9%	13.3%	6.5%	9.6%

the SMC rotor poles, necessitating careful quality control. Nonetheless, the tested results indicate that the 3-D FEA models represent a good correlation between the prototyped machines of different topologies in terms of air-gap flux from back-EMF and static torque.

2) ON-LOAD MEASUREMENT

Dynamic characteristics are also tested at different loads and speeds. The current ripples of the line current are filtered using a high-pass filter to accurately measure losses under sinusoidal excitation. Mechanical losses are calibrated using dummy rotors to obtain the electromagnetic torque, as shown in Fig. 28. The loads are varied at approximately 1.25 Nm, 2.5 Nm, and 5 Nm. The difference between measured and 3-D FEA calculated torque ranged from 9% to 15%. One contributing factor to his discrepancy is underestimation of mechanical losses, as the dummy rotors do not account for the increased axial loading after assembly.

TABLE 5. Measured Performance at Different Currents (1,000 RPM).

Parameter	SMAPFM			CPAFPM		
Torque (Nm)	1.24	2.51	5.01	1.24	2.50	5.05
Line current amplitude (A)	5.96	11.77	23.93	8.47	17.29	39.48
Losses (W)	12.56	30.77	111.9	14.86	57.66	308.2
Efficiency (%)	91.18	89.48	82.38	89.73	81.95	62.95

The line current amplitudes of the SMAFPM machine for three loads are approximately 6 A, 12 A, and 24 A,
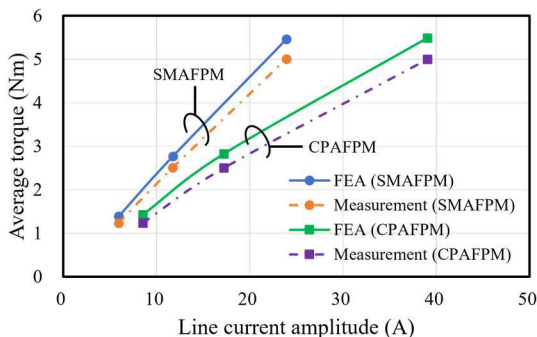
FIGURE 28. Measured and FEA calculated torque-current characteristics.

TABLE 6. Measured Performance at Different Currents (2,000 RPM).

Parameter	SMAPFM			CPAFPM		
Torque (Nm)	1.22	2.54	5.02	1.23	2.49	5.02
Line current amplitude (A)	6.05	11.86	24.27	8.39	17.25	39.52
Losses (W)	19.84	40.23	127.1	16.81	63.22	313.9
Efficiency (%)	92.79	92.97	89.21	93.83	89.38	77.01

which correspond to the current densities of 2.5 A/mm^2, 5 A/mm^2, and 10 A/mm^2, respectively. In contrast, the CPAFPM machine produces the same torque, with current densities of 3.6 A/mm^2, 7.3 A/mm^2, and 16.5 A/mm^2, respectively. The overload operation under natural cooling is typically limited to 10 A/mm^2, which corresponds to a peak torque of 3.28 Nm for the CPAFPM machine. As a result, the torque density of the CPAFPM machine is approximately 36% lower than that of the CMAFPM machine.

Tables 5 and 6 show measured losses and efficiencies at different loads for both machines at 1,000 rpm and 2,000 rpm, respectively. At 1,000 rpm, the CPAFPM machine always shows lower efficiency due to high portion of copper losses at all load levels, even at a light load of 1.25 Nm, resulting in poor efficiency of 62.95% at the overload torque of 5 Nm. Conversely, the losses in the SMAFPM machine are more balanced at 1.25 Nm, indicating a peak efficiency of 91.18%. At 2,000 rpm, iron losses approximately double due to increased hysteresis losses in the stator core. The CPAFPM machine shows lower iron losses at 1.25 Nm, leading to higher efficiency of 93.83%, compared to 92.79% for the SMAFPM machine. However, the SMAFPM machine reaches its highest efficiency at 2.5 Nm, whereas efficiency of the CPAFPM machine declines as the load increases.

C. COMPARISON OF MATERIAL COSTS
Based on the comparative study, the CPAFPM machine inherently demonstrates lower efficiency at rated and heavy load due to its lower magnetic loading. The weight of the active parts for both machines is roughly 1.14 kg, resulting in a peak torque density of 4.39 Nm/kg for the SMAFPM machine and a 36% lower torque density of 2.88 Nm/kg

for the CPAFPM machine. Therefore, the conversion of SM to CP topology is more suitable for machine systems that includes a gearbox, allowing the machine to be designed for higher speeds. Consequently, the simple replacement of the PMs with SMCs allows the machine's main operating region to shift, while maintaining the same components (coils, cores, and PMs) and manufacturing process (gluing SMCs instead of PMs).

For a quantitative cost analysis, the cost per kilogram of each active material is summarized in Table 7.

TABLE 7. The cost per kilogram of active materials.

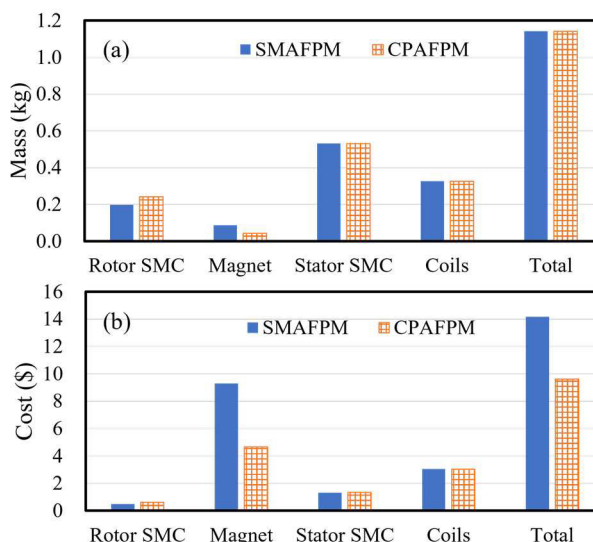|	Copper	SMC	Magnet
Cost ($/kg)	9.3	2.5	105.7

FIGURE 29. (a) Mass and (b) cost of active materials.

The cost of each component is estimated based on the mass of the components presented in Fig. 29(a). Despite the higher mass of stator/rotor cores and coils, the PM content primarily determines the total cost of the machine, as shown in Fig 29(b). The CPAFPM machine shows a 47% lower cost, which closely aligns with its reduced torque density ratio. The estimated cost is based on a simple cost analysis that considers only the cost of the raw materials, excluding both production and assembly costs. Additionally, the cost study does not account for price variations due to supply chain factors or potential increases from additional processes, such as magnet segmentation.

V. CONCLUSION
This article presents a comparative study of surface-mounted and consequent pole topologies for Axial Flux Machines. The inherent inclusion of even harmonics in air-gap flux for the CP topology is studied to give insight into selecting

the suitable winding configuration. The direct replacement of half magnets by SMC poles offers 70% of the torque production, with only 50% of the magnet, improving the torque per Permanent Magnet volume.

The armature inductance of two topologies is compared, and the effect of the armature reaction on the saturation and consequent load-dependent characteristics are studied. The higher d-axis inductance of the CPAFPM machine can benefit from enhanced flux-weakening capability, but high q-axis inductance can make a risk of saturation, especially for stator cores, leading to lower overload capability in terms of torque and power factor.

Nonetheless, the low magnetic loading of the CPAFPM topology can offer the benefit of lower iron loss and magnet eddy current loss at high speeds and in the low to medium torque regions. The SMAFPM and CPAFPM topologies are comprehensively compared in efficiency maps to identify their respective highest efficiency points. The SMAFPM machine demonstrates higher efficiency at higher torque and lower speed regions compared to the CPAFPM machine.

Four operating points are selected to provide an understanding of the operating regions where each topology can achieve better performance. At the same power level, the CPAFPM topology can be preferably employed for design targets of higher speed and lower torque, where comparable efficiency can be achieved, providing guidance for selecting the operating point while reducing the cost of electric motors.

Alongside simulation studies, both machines were fabricated, and the back-EMF and static torque obtained from 3-D FEA were confirmed to validate the accuracy of the simulations. The CPAFPM machine under study utilizes a shared stator core and rotor back iron core to minimize manufacturing effort. To further improve the performance of the CPAFPM topology, our future research will focus on providing viable options for machines that utilize fewer rare-earth PMs, as outlined below:

- Optimization of PMs and SMC poles to better exploit reluctance torque and maximize torque relative to cost.
- Exploration of various configurations, such as spoke-type, vernier-type, and novel topologies.
- Redesign of the CPAFPM machine to achieve the same peak torque as the SMAFPM, with a detailed comparison of performance metrics such as demagnetization rate, torque density, flux-weakening capability, and driving cycle efficiency.

ACKNOWLEDGMENT

REFERENCES

[1] D. F. de Souza, P. P. F. da Silva, I. L. Sauer, A. T. de Almeida, and H. Tatizawa, "Life cycle assessment of electric motors—A systematic literature review," *J. Cleaner Prod.*, vol. 456, Jun. 2024, Art. no. 142366.

[2] J. M. Tabora, M. E. De Lima Tostes, U. H. Bezerra, E. O. De Matos, C. L. P. Filho, T. M. Soares, and C. E. M. Rodrigues, "Assessing energy efficiency and power quality impacts due to high-efficiency motors operating under nonideal energy supply," *IEEE Access*, vol. 9, pp. 121871–121882, 2021.

[3] H. Hua and Z. Q. Zhu, "Investigation on symmetrical characteristics of consequent-pole flux reversal permanent magnet machines with concentrated windings," *IEEE Trans. Energy Convers.*, vol. 37, no. 3, pp. 1815–1824, Sep. 2022.

[4] L. Shao, R. Navaratne, M. Popescu, and G. Liu, "Design and construction of axial-flux permanent magnet motors for electric propulsion applications—A review," *IEEE Access*, vol. 9, pp. 158998–159017, 2021.

[5] R. Kumar, Z.-Q. Zhu, A. Duke, A. Thomas, R. Clark, Z. Azar, and Z.-Y. Wu, "A review on transverse flux permanent magnet machines for wind power applications," *IEEE Access*, vol. 8, pp. 216543–216565, 2020.

[6] F. Nishanth, J. Van Verdeghem, and E. L. Severson, "A review of axial flux permanent magnet machine technology," *IEEE Trans. Ind. Appl.*, vol. 59, no. 4, pp. 3920–3933, Aug. 2023.

[7] C. Jenkins, S. Jones-Jackson, I. Zaher, G. Pietrini, R. Rodriguez, J. Cotton, and A. Emadi, "Innovations in axial flux permanent magnet motor thermal management for high power density applications," *IEEE Trans. Transp. Electrific.*, vol. 9, no. 3, pp. 4380–4405, Sep. 2023.

[8] M. Polat, A. Yildiz, and R. Akinci, "Performance analysis and reduction of torque ripple of axial flux permanent magnet synchronous motor manufactured for electric vehicles," *IEEE Trans. Magn.*, vol. 57, no. 7, pp. 1–9, Jul. 2021.

[9] W. Li, P. Song, S. Mukundan, B. De Silva Guruwatta Vidanalage, G. Spehar, V. Russalian, S. Reaburn, and N. C. Kar, "Structural analysis of single-sided axial-flux permanent magnet machines with different magnetic materials," *IEEE Trans. Magn.*, vol. 57, no. 2, pp. 1–5, Feb. 2021.

[10] Z. Hao, Y. Ma, P. Wang, G. Luo, and Y. Chen, "A review of axial-flux permanent-magnet motors: Topological structures, design, optimization and control techniques," *Machines*, vol. 10, no. 12, p. 1178, Dec. 2022.

[11] N. Ahmed and G. J. Atkinson, "A review of soft magnetic composite materials and applications," in *Proc. Int. Conf. Electr. Mach. (ICEM)*, Sep. 2022, pp. 551–557.

[12] R. Tsunata, M. Takemoto, S. Ogasawara, T. Saito, and T. Ueno, "SMC development guidelines for axial flux PM machines employing coreless rotor structure for enhancing efficiency based on experimental results," *IEEE Trans. Ind. Appl.*, vol. 58, no. 3, pp. 3470–3485, May 2022.

[13] R. Manko, R. Dmytro, M. Vukotić, U. Rupnik, D. Miljavec, and S. Čorović, "A review of manufacturing technologies of soft magnetic composites for electric machines," in *Proc. IEEE 5th Int. Conf. Modern Electr. Energy Syst. (MEES)*, Sep. 2023, pp. 1–4.

[14] M. C. Kulan, N. J. Baker, K. A. Liogas, O. Davis, J. Taylor, and A. M. Korsunsky, "Empirical implementation of the steinmetz equation to compute eddy current loss in soft magnetic composite components," *IEEE Access*, vol. 10, pp. 14610–14623, 2022.

[15] J. Washington, S. Jordan, and L. Sjöberg, "Methods for the construction of single-sided axial flux machines using soft magnetic composites," in *Proc. IEEE Energy Convers. Congr. Expo. (ECCE)*, Portland, OR, USA, Sep. 2018, pp. 3278–3285.

[16] S. Liu, T. Li, J. Luo, Y. Yang, C. Liu, and Y. Wang, "Core loss analysis of soft magnetic composites based on 3D model considering temperature influence," *IEEE Access*, vol. 9, pp. 153420–153428, 2021.

[17] R. Tsunata, M. Takemoto, J. Imai, T. Saito, and T. Ueno, "A proposal of an axial-flux permanent-magnet machine employing SMC core with tooth-tips constructed by one-pressing process: Improving torque and manufacturability," *IEEE Access*, vol. 11, pp. 109435–109447, 2023.

[18] J. Qi, Z.-Q. Zhu, L. Yan, G. W. Jewell, C. Gan, Y. Ren, S. Brockway, and C. Hilton, "Effect of pole shaping on torque characteristics of consequent pole PM machines," *IEEE Trans. Ind. Appl.*, vol. 58, no. 3, pp. 3511–3521, May 2022.

[19] L. Jia, K. Lin, M. Lin, W. Le, and S. Wang, "Comparative analysis of dual-rotor modular stator axial-flux permanent magnet machines with different rotor topologies," *IEEE Trans. Appl. Supercond.*, vol. 31, no. 8, pp. 1–5, Nov. 2021.

[20] T. Takahashi, M. Takemoto, S. Ogasawara, T. Ogawa, H. Arita, and A. Daikoku, "Development of a consequent-pole-PM-type axial-gap motor with DC field winding," *IEEE Trans. Ind. Appl.*, vol. 57, no. 5, pp. 4363–4375, Sep. 2021.

[21] L. Jia, M. Lin, W. Le, and S. Wang, "Influence of different rotor structures on axial flux permanent magnet machine with segmented stator," in *Proc. IEEE Int. Conf. Appl. Supercond. Electromagn. Devices (ASEMD)*, Oct. 2020, pp. 1–2.

[22] M. Jia, Y. Feng, K. Huang, C. Xia, Y. Li, and S. Huang, "Research on flux-focusing axial-flux consequent-pole Vernier permanent magnet machine based on the global tooth chamfering," in *Proc. 26th Int. Conf. Electr. Mach. Syst. (ICEMS)*, Nov. 2023, pp. 3274–3279.

[23] Q. Chen, D. Liang, S. Jia, Q. Ze, and Y. Liu, "Analysis of winding MMF and loss for axial flux PMSM with FSCW layout and YASA topology," *IEEE Trans. Ind. Appl.*, vol. 56, no. 3, pp. 2622–2635, May 2020.

[24] C. Wang, Z. Zhang, Y. Liu, W. Geng, and H. Gao, "Effect of slot-pole combination on the electromagnetic performance of ironless stator AFPM machine with concentrated windings," *IEEE Trans. Energy Convers.*, vol. 35, no. 2, pp. 1098–1109, Jun. 2020.

[25] *Somaloy® Prototyping Material, SPM*, document 1334HOG, Höganäs AB, Apr. 2016.

[26] A. M. EL-Refaie, "Fractional-slot concentrated-windings synchronous permanent magnet machines: Opportunities and challenges," *IEEE Trans. Ind. Electron.*, vol. 57, no. 1, pp. 107–121, Jan. 2010.

[27] N. Taran, G. Heins, V. Rallabandi, D. Patterson, and D. M. Ionel, "Evaluating the effects of electric and magnetic loading on the performance of single- and double-rotor axial-flux PM machines," *IEEE Trans. Ind. Appl.*, vol. 56, no. 4, pp. 3488–3497, Jul. 2020.

[28] D. C. R. Pinto, H. Xu, and R. W. De Doncker, "Accurate FEA-based modeling of IPMSMs operating under high magnetic utilization," in *Proc. 25th Int. Conf. Electr. Mach. Syst. (ICEMS)*, Nov. 2022, pp. 1–6.

RAJESH KUMAR was born in Umarkot, Pakistan. He received the B.E. degree in industrial electronics from the Institute of Industrial Electronics Engineering, Karachi, Pakistan, in 2014, the M.E. degree in electrical engineering from the University of Tun Hussein Onn Malaysia, in 2017, and the Ph.D. degree in electrical engineering from The University of Sheffield, in 2022. Currently, he is a Senior Application Specialist with Alvier Mechatronics, Sweden. His research interests include electromagnetic design, modeling, and optimization of electrical machines for various applications.

DAE YONG UM (Member, IEEE) received the B.S., M.Sc., and Ph.D. degrees in electrical engineering from Pusan National University, Busan, South Korea, in 2017, 2019, and 2023, respectively. From 2023 to 2024, he joined as a Research Associate with the Electric Power Group, Newcastle University, U.K. Currently, he is an Assistant Professor with Gyeongsang National University, South Korea. His research interests include numerical modeling and analysis of electromagnetic fields for electric machines, non-destructive testing, and wireless power transfer.

LARS SJÖBERG was born in Helsingborg, Sweden. He received the M.Sc. degree in electrical engineering and the Tech.Lic. degree from the Department of Industrial Electrical Engineering and Automation, LTH/Lund University, Lund, Sweden, in 1992 and 1996 respectively. He was with the companies Emotron AB and Danaher Corporation as an Electric Machine Designer focusing on the design and control of switched reluctance, induction, and PM machines. From 2003 to 2008, he was managing the Electro and Power Supply Group, Swedish Railway Training Centre. He joined Höganäs AB, in 2009, as an Electric Motor Application Specialist, where he also held a position as an Application Engineering Manager. Since 2023, he has been the Head of the System Simulation Team, Alvier Mechatronics, AB (an engineering service company within the Höganäs Group), where his responsibility is design and simulation methodology and services targeting electric motors and passive components.

TUSHAR BATRA received the B.E. degree in electrical engineering from Punjab Engineering College, Chandigarh, India, in 2008, the master's degree in electric power and wireless power transfer for electric vehicles from RWTH, Aachen, Germany, in 2012, and the Ph.D. degree in electric power and wireless power transfer for electric vehicles from Aalborg University, Aalborg, Denmark, in 2015. Afterwards, he was a Power Plant Engineer with Alstom Power, Noida, India, from 2008 to 2010. During his Ph.D., he was a six-month a Visiting Scholar with EMC Laboratory, KAIST, Daejeon, South Korea, in 2014. After Ph.D., he pursued a Postdoctoral Fellowship, from 2016 to 2017, focused on Gate Driver Insulation Coordination for HV Wideband Gap Devices from FRE EDM System Center, North Carolina State University, Raleigh, USA. He worked on the design and development of Optical Isolated Current Transformers and Shunts at ABB HVDC, Ludvika, Sweden, from 2017 to 2018. He joined Höganäs AB, Höganäs, Sweden thereafter as a Research and Development Engineer for Inductors. After internal promotions, he is currently with Höganäs Group Daughter Company, Alvier Mechantronics AB as Lead Electromagnetic Innovation, focusing on passive components, magnetic materials, and components characterization and motor design.

GLYNN ATKINSON is a Reader of electrical machine and the Head of the Electrical Power Research Group. His research interests include the design of three-dimensional machine topologies using soft magnetic composites, power dense fault tolerant machines for aerospace, and the design and analysis of electrical machines and their manufacture for a wide variety of domestic and industrial applications. He has worked with many industrial partners, and leads the Alvier Research Centre and FEMM hub at Newcastle.

• • •